Fit-for-Purpose Approach for the Detection and Analysis of Earthquake Surface Ruptures Using Satellite Images

Yire Choi [ID], Jin-Hyuck Choi [ID], and Yeonju Choi [ID]

Abstract—Coseismic surface ruptures are the ground truth of earthquake rupture along faults, and detailed mapping of earthquake surface ruptures provides an opportunity to understand the relationship between earthquakes and faults. One of the most effective tools for mapping earthquake surface ruptures is the use of remote sensing data, such as high-resolution satellite imagery. This study proposes a crack detection model based on deep learning and analysis tools to extract the geometrical characteristics of surface rupture using high-resolution satellite imagery (Pléiades-1B) for an earthquake that occurred in the Bulnay region of Mongolia. By comparing the prediction result with a line map of the previous study (Choi, 2018), it was possible to confirm the reliability of the fault detection. The model achieved a rupture detection accuracy of approximately 90% and an extraction of characteristic features of crack error level of 5% or less. To assess the broad applicability of the proposed model regardless of image size, we evaluated the model performance through quantitative and qualitative methods. The model accurately calculated essential characteristics, such as the orientation and length of a diverse range of surface ruptures. These results confirm the general effectiveness of the proposed model in detecting and characterizing surface ruptures caused by earthquakes. The suggested model for automated target detection utilizing satellite imagery can serve as a fit-for-purpose solution for conducting field surveys and acquiring fundamental earthquake-related data. The proposed model can provide valuable insights into the aftermath of seismic events by identifying a range of surface ruptures and deformations induced by earthquakes.

Index Terms—Coseismic surface ruptures, deep learning, earthquake fault mapping, morphology feature extraction, satellite imagery.

Yire Choi is with the Active Tectonics Research Center, Korea Institute of Geoscience and Mineral Resources, Daejeon 34132, South Korea (e-mail: ir_1254@kigam.re.kr).

Jin-Hyuck Choi is with the Active Tectonics Research Center, Korea Institute of Geoscience and Mineral Resources, Daejeon 34132, South Korea, and also with the Department of Geological Science, University of Science and Technology, Daejeon 34113, South Korea (e-mail: cjh9521@kigam.re.kr).

Yeonju Choi is with the Satellite Application Division, Korea Aerospace Research Institute, Daejeon 34133, South Korea (e-mail: choiyj@kari.re.kr).

I. INTRODUCTION

AN EARTHQUAKE is a sudden slip of a fault. In continental earthquakes greater than magnitude 6, the slip surface reaches the ground surface, resulting in permanent surface ruptures. In addition to instrumental seismicity, geodetic measurements, and numerical modeling, mapping of earthquake surface ruptures provides an opportunity to understand the earthquake rupture processes and their relations with the inherited faults [2], [3]. By mapping the cumulative surface ruptures associated with multiple earthquakes, researchers can investigate the history of fault ruptures over multiple earthquake events [4]. Both coseismic and cumulative surface deformation resulting from earthquake ruptures are crucial for comprehending how significant active faults accommodate crustal deformations in the Earth. Moreover, quantitative parameters of earthquake surface ruptures are utilized for assessing seismic hazards, including investigating earthquake cycle models and estimating the maximum magnitude that a future earthquake in a given fault system could attain.

A. Related Work

Before the 1990s, mapping earthquake surface ruptures were conducted mainly through field observations and imagery analysis using aerial photos [5], [6]. Although a field survey is one of the most accurate methods to map the earthquake surface ruptures, it could be a highly time-consuming investigation considering that surface ruptures occur within up to a few hundred kilometers depending on the earthquake size [7]. Significant advancements in mapping earthquake surface ruptures have been achieved through advances in remote sensing techniques (e.g., interferometric synthetic aperture radar, InSAR). These advances emerged in the early 2000s, coinciding with the utilization of high-resolution satellite images in the field of earthquake sciences [8]. High-resolution topographic data that are mainly generated vis the structure-from-motion approach as well as light detection and range have now become the main tools to map the earthquake surface ruptures [9], [10], [11]. More recently, it is possible to map coseismic surface deformation using technics that directly correlate pre and postearthquake images or digital elevation model (DEM) [12], [13] [14]. In particular, satellite data became increasingly available due to high spatial resolution and extensive data acquisition over most regions of the Earth. Indeed, for destructive earthquakes involving surface faulting,

there is a growing trend to use satellite-based InSAR and image correlation together with seismic and geodetic data to understand the earthquakes [15], [16].

Deep learning and computer vision technologies have recently been utilized in the field of tectonic-geomorphic investigations based mainly on crack detection using remote sensing data. Mattéo et al. [17] developed the model based on U-Net [18] for automatically mapping tectonic faults in optical images and topographical data and their architecture was based on one developed by [19]. Despite being trained on low-quality and small-sized datasets, their model can be strongly generalized and applied to different types of image data. Jafrasteh et al. [20] proposed an automated fractures and faults mapping method using a generative adversarial network model to predict small fractures. Building on previous research, the authors in [17], [19], and [21] proposed an improved deep learning approach to identify and map faults and fractures through high-resolution optical images and topographic data. Their method, focused on identifying long-lived geological faults, but did not address recent surface ruptures caused by earthquakes. Meanwhile, a deep learning-based crack detection model was employed to detect coseismic surface ruptures using postevent unmanned aerial vehicle (UAV) images obtained from the M 7.4 Maduo earthquake in China [22], [23]. Chen et al. [22] proposed a deep learning method to identify cracks and developed a semantic segmentation network, which efficiently mapped the major surface ruptures caused by the earthquake, despite some false and missed identifications. Yu et al. [23] proposed a remote sensing-based automatic crack detection framework that focuses on densely distributed cracks to detect coseismic ruptures caused by earthquakes. The framework integrates a novel terrain surface crack detection neural network named Crack-CADNet, which outperformed recent CNN-based methods in detecting cracks.

B. Our Proposed Contribution

Identifying earthquake surface ruptures using deep learning is challenging, owing to the complex background of postearthquake images and the varied and complicated shapes of the ruptures, which can appear in any position and direction. The Bulnay region's earthquakes exhibit surface ruptures distributed across different geographic regions, further complicating the identification task. To achieve efficient, precise, and intelligent detection of surface rupture caused by postearthquake events, this study, pertaining to the 1905 earthquakes in the Bulnay region of Mongolia, not only presents a fit-for-purpose approach for a deep learning-based crack detection model but also introduces a model for automatic analysis of the detected cracks' geology/geomorphology features. The suggested model represents the first attempt to accurately detect surface rupture using high-resolution satellite imagery (Pléiades-1B). The surface ruptures were precisely detected with high accuracy, and quantitative characteristic information was calculated. Through comparison with previous mapping results by manual imagery and field observations [1], mapping information by the proposed model in the test area was clearly verified. The utilization of high-resolution satellite images to map widely distributed earthquake surface ruptures has the advantage of being able

to conduct mapping quickly with a single satellite image, particularly in hard-to-work-in regions, with the elimination of subjective interpretation by experts. Also, the finding of along-fault variations in rupture geometry and/or complexity, which is a typical feature of the surface ruptures associated with large earthquakes [5], [24], provides an opportunity to interpret rupture behaviors as the first stage investigation and to establish a follow-up survey strategy, such as field survey site selection. Therefore, combining high-resolution satellite imagery and deep learning algorithms, which enables rapid and accurate fault detection in large-scale regions, and a quantitative analysis model which provides morphology features of detected cracks are expected that it could provide a crucial integrated solution for more comprehensive and efficient postearthquake investigations. In particular, only a crack was detected with high accuracy by learning a model based on a random augmentation technique and a strong penalty loss function to the undesired target. We believe that the proposed model, which also provides the analysis result of the crack with coordinate information, can be highly effective in postearthquake investigations and can support disaster management by providing significant information for damage assessment and identifying high-risk areas for geohazards, such as landslides and liquefaction. This can aid in determining the optimal allocation of resources and prioritizing response efforts. Furthermore, the proposed model can contribute to improving the accuracy and efficiency of early warning systems, which are essential for minimizing the impact of future earthquakes and other natural disasters. This article contributes to literature in four major respects as follows.

1) Earthquake rupture analysis is a very challenging task due to its complex structure and background, and we have proposed an optimized method for this purpose.
2) Using high-resolution satellite images, we proposed a deep learning model including an optimized loss function and augmentation technology for detecting surface rupture by an earthquake in the Bulnay region of Mongolia.
3) A morphological analysis model that segments the detected cracks into individual cracks and accurately extracts morphological information is proposed.
4) Proposed models can provide a crucial integrated solution for comprehensive and efficient postearthquake investigations.

The rest of this article is outlined as follows: Section II introduces a dataset and study area and describes the proposed methods in detail. Section III presents the results and analyses of our approach. Discussion is present in Section IV. Finally, Section V concludes this article.

II. METHODOLOGY

A. Study Area and Dataset

Mongolia is a tectonically active intracontinental region, with seismicity mostly associated with regional deformations related to the convergence of the Indo-Eurasia plate [25], [26], as shown in Fig. 1(a). In 1905, the largest continental earthquake sequence ever recorded struck the Bulnay fault system in northwest Mongolia: 1) the July 9th, M $\sim$ 8, Tsetserleg earthquake; 2) the July 23 rd, M > 8 Bulnay earthquake. These
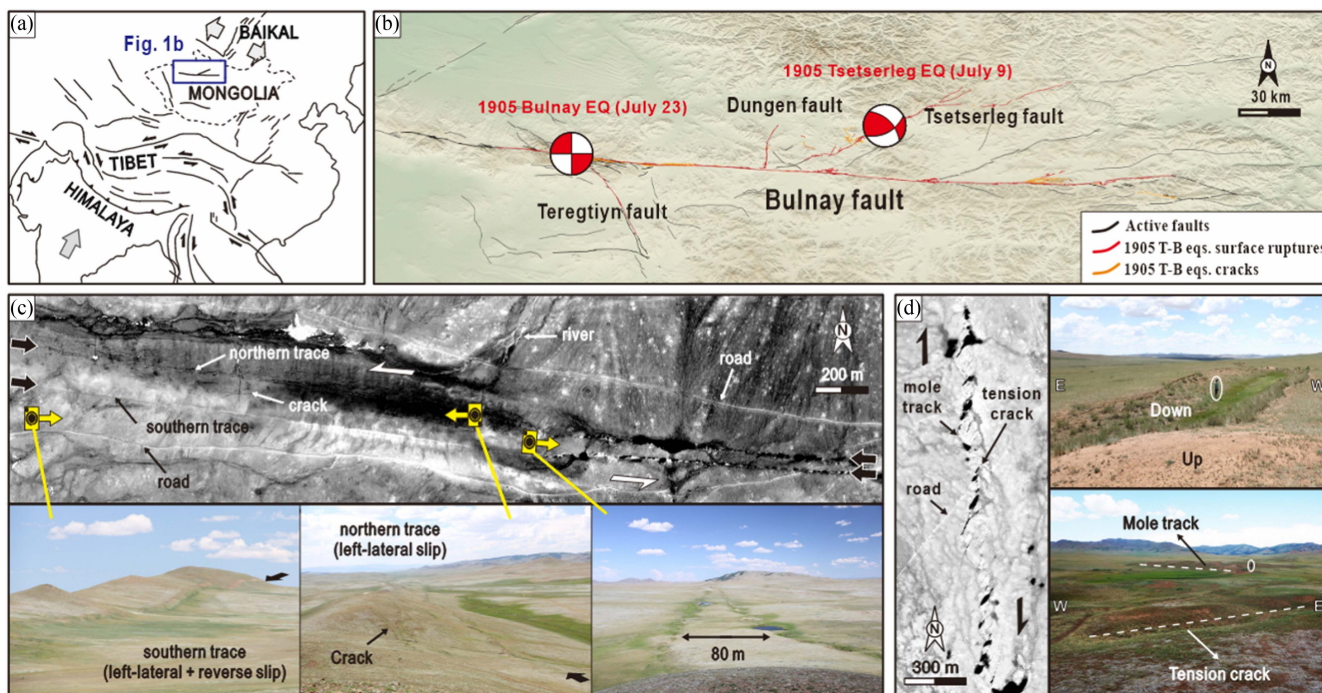
Fig. 1. (a) Simplified tectonic map around Mongolia. (b) Structural map of the Bulnay fault system. Fault traces marked by red and orange indicate the coseismic surface ruptures and cracks associated with the 1905 M ∼ 8 Tsetserleg and Bulnay earthquakes. (c) Rupture section along the western Bulnay fault. Both Pléiades imagery and field observations indicate the earthquake surface ruptures' complex geometry and two-parallel traces. (d) Rupture section along the Dungen fault that is geometrically highlighted by en echelon cracks and mole tracks without a through-going rupture trace on the Pléiades images and in the field. In addition to the earthquake surface ruptures, other linear features, such as rivers and roads appear on the Pléiades satellite images. All figures were modified from [1].

two successive events, referred to as the 1905 Tsetserleg–Bulnay earthquake sequence (1905 T–B eqs), caused surface ruptures with a total length of at least 676 km [Fig. 1(b)]. Choi et al. [1] conducted detailed mapping of surface ruptures associated with the 1905 T-B eqs based on submeter ground sampling distance, 0.5-m optical satellite "Pléiades" imagery, and field surveys. We note that Mongolia has almost no erosion and deposition due to high mountain dry climate conditions, and the earthquake surface ruptures are well preserved to the present day. Mapping results by Choi et al. [1] indicate that the rupture geometry is complicated, such as en echelon cracks, mole tracks, fault jogs and/or bends, and fault branches, similar to other strike-slip earthquakes, and the horizontal offset was about 6 m along the main Bulnay fault and about 2 m along the other branch faults.

The main target of this study is the surface ruptures on the central-western section of the Bulnay and the Dungen fault [Fig. 1(b)]. These two sections were designated because the rupture geometry is remarkably complex among the entire surface ruptures [Fig. 1(c) and (d)]: 1) the primary rupture strand consists of en echelon tension cracks and mole tracks, 2) pull-apart or pressure-ridge associated with fault jogs between subparallel ruptures, 3) local compressional deformation caused by the change of the azimuth of the main fault, and 4) two parallel strands with strike-slip rupture. The study utilized Pléiades-1B images in both panchromatic and pan-sharpened formats, with a resolution of 0.5 m. The selected datasets had less than 10 % cloud coverage and a tilt angle range of 12–19°. The Bulnay and Dungen fault areas are covered with snow for most of the
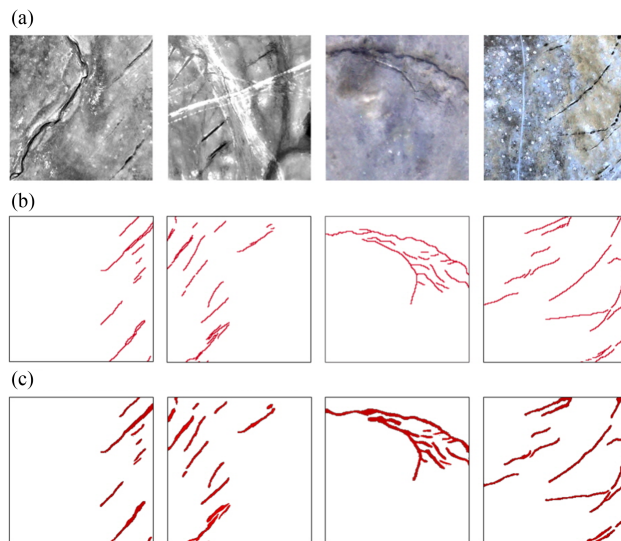

Fig. 2. Selection of the dataset: Satellite images, line maps, and refined line map as ground truth. (a) Satellite images: panchromatic, pan-sharpend (b) Line map: Training reference. (c) Refined line map: Comparitive reference.

year, which makes it difficult to identify surface ruptures using satellite imagery. Therefore, to mitigate this seasonal effect, we utilized satellite images captured at a specific time when surface ruptures can be detected. The image was taken around May 2013 and was used in a previous study by Choi et al. [1].

Examples of the datasets used are shown in Fig. 2. The mask images displaying the cracks in the satellite image (first
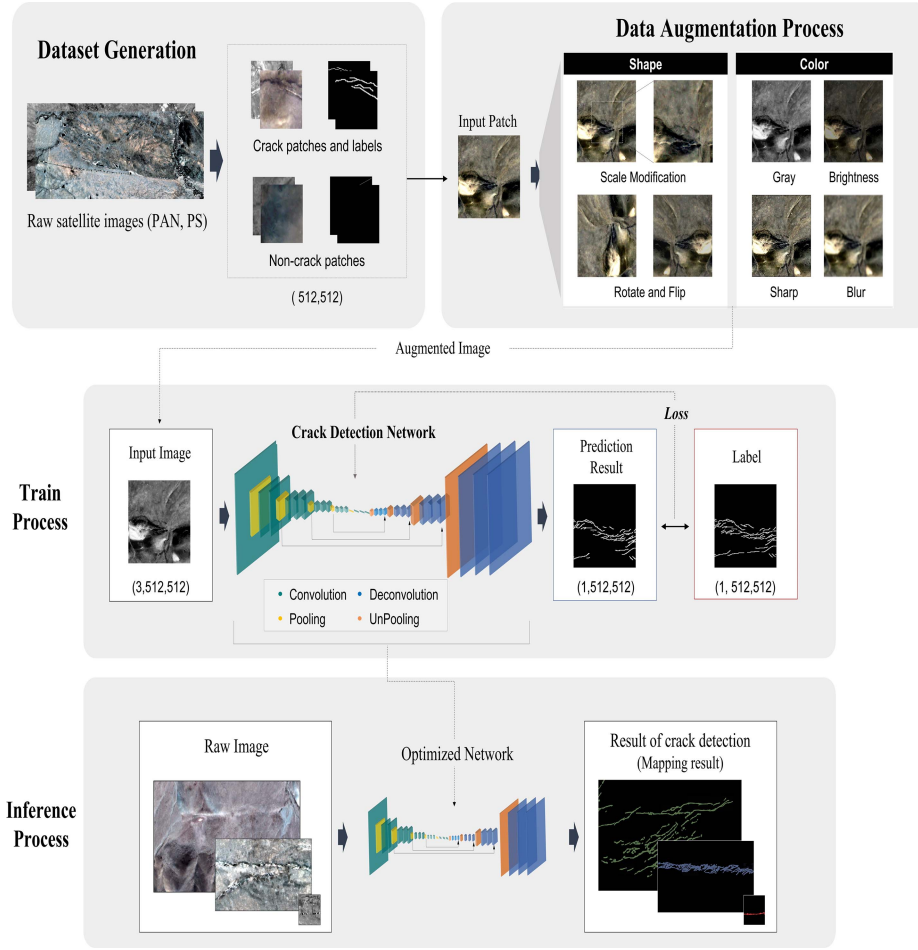
Fig. 3. Proposed surface rupture detection model architecture and process flow.

row) were created with lines of equal thickness (second row) for the purpose of training ground truth, based on the manual sketches provided in the result of [1]. The refined line maps are additionally created to evaluate how exactly the actual crack shape can be detected with respect to the test images (third row). The initial line map was modified by experts to reflect the actual shape and thickness that can be displayed in colored form according to the rupture area.

Meanwhile, in the collected dataset, the desired target, namely, cracks, is distributed at a very low rate in the generated patch. To ensure effective feature learning, the usefulness of each patch was determined by calculating the crack ratio using a statistical method. We assume that there are n raw images, and each image size is H(height) $\times$ W(width). The number of crack pixels in ith raw image is expressed as N_{crack}^{i} and N_{image}^{i} is the number of pixels in the image. The average ratio of all crack pixels to pixels in all images, R_{image} is defined as

$$R_{\text{image}} = \frac{\sum_{i=1} N_{\text{crack}}^{i}}{\sum_{i=1} N_{\text{image}}^{i}} = \frac{\sum_{i=1} N_{\text{crack}}^{i}}{n(W \times H)}. \tag{1}$$

Next, raw images were divided into patches of the same size (512×512) with a stride of 200 pixels by the overlap sliding window method. We defined the number of crack pixels as N_{crack}^{ij}

and the number of all pixels as N_{image}^{ij} in the jth patch in the ith raw image. Finally, the portion of crack pixel to all pixels in the jth patch in the ith image is expressed as

$$R_{\text{patch}}^{ij} = \frac{N_{\text{crack}}^{ij}}{N_{\text{image}}^{ij}}. \tag{2}$$

Only patches satisfying the condition $R_{\text{patch}}^{ij} \geq R_{\text{image}}$, and a patch containing a larger ratio of crack pixels than the average ratio for all raw images, were selected. Through this condition, we constructed the training set with around 6000 patches. It was composed of training, verification, and evaluation sets at a ratio of 8:1:1 among the entire data. The generated final patches were converted to [0–1] value through the min-max normalization method.

B. Crack Detection Network

In this section, we describe a deep learning network designed for detecting various types of surface ruptures resulting from a T–B earthquake. The network utilized in this study is a fully convolutional network (FCN) based on the VGG-16 [27] segmentation model, as illustrated in Fig. 3, which has demonstrated excellent segmentation performance in previous research [28].

The convolution part consists the five convolution layers followed by an ReLU and max pooling layers for down-sampling. To obtain output with the same size as the original images, we add four decoder layers and upsampling layers are followed by convolutional layers to produce dense features with finer resolution. This symmetrical structures of the encoder and decoder is connected with skip connections which takes outputs after each max pooling layer in the VGG-16. At the end of the step, upsampling is performed with a feature map that contains only high-dimensional information, so coarse information could be omitted. Therefore, the role of skip connection is to deliver the coarse information to the network so that all features from low-level to high-level can be combined. All parameters of the network learned and fine-tuned using Adam optimizer and the learning rate starts at 2×10^{-4}, and the cosine annealing technique is applied as a scheduler to update the rate during training. Meanwhile, this study focused on segmenting the rupture in a satellite image, which can be viewed as a binary problem. The input dimension of the network is (3, 512, 512), corresponding to the pan-sharpened image with red, green, and blue (RGB) bands. In the case of panchromatic, we expanded the original image to three channels. The output dimension is (2, 512, 512), consisting of two classes: class 1 represents the rupture, which is the detection target, while class 0 corresponds to the background (e.g., road, mountain, and tree) excluding cracks. As explained in Section II-A, only images that satisfied the criteria were selected, and the training dataset was divided into patches. However, a class imbalance problem still existed during training due to the difference in the ratio between the two classes. For instance, when the model learns about the major class (background as nondesired target), the relatively minor class (crack as the desired target) may yield an increase in false positives. To address this issue, we applied a stronger penalty for misclassifying the target class than the background class and emphasized the importance of the crack class for improving overall detection performance. The weighted softmax cross-entropy (WSCE) loss function defined in (3) was used, where the weight for the target class was increased

$$\text{SCE}(p_c) = -\alpha_c \log(p_c) \tag{3}$$

$$p_c = \begin{cases} p & y = 1 \\ 1 - p & y = 0. \end{cases} \tag{4}$$

Here, p_c in (4) is the estimated probability for crack $p \in [0,1]$, and c is the number of class, $c = 2$ (crack = 1, background = 0). As mentioned above, in order to minimize the imbalance effect between classes, the class weight factor α_c is adopted, as defined in the following:

$$\begin{cases} \alpha_1 = 0.5 \times (1 + e^{-10}) \\ \alpha_2 = 10 - \alpha_1. \end{cases} \tag{5}$$

Meanwhile, to address the lack of training data and demonstrate robust detection performance in various environments, we employed rand augmentation [29] in the proposed model. This technique is known to perform best in data augmentation policy search with only two parameters (N, M), where N is the number of augmentations to be applied, and M is the magnitude

of the augmentation to be applied. We applied rand augmentation to the next step of the training data load, with modifications applied in two categories: 1) color (contrast, brightness, sharpness, equalization, invert, etc.) and 2) shape (flip, rotation, shear, translation, resize, etc.). A total of 12 types (N) of modifications were applied, and the augmentation magnitude (M) was set to 14.

III. RESULTS

In this study, we evaluated the performance of the developed surface rupture detection model using various methods. First, we conducted a visual comparison between the detected results from the test patches of the same size and the refined line map to determine how accurately the actual rupture shapes were detected. Next, we calculated the accuracy metric for about 10% of the entire dataset for the detection performance and compared it with other algorithms. Finally, we introduced a proposed model capable of extracting topographic features based on the detected cracks and analyzed the accuracy of the extracted information compared to previous research results. Through this multifaceted analysis, we confirmed the potential of the developed model as an effective analysis tool for earthquake-prone areas.

A. Performance of the Crack Detection

The performance of the model is evaluated using precision, recall, and F1 score. Precision measures the degree of actual correct predictions out of the total predictions made, while recall measures the accuracy of actual cracks that were correctly classified. The F1 score is the average value of arithmetic harmonization for recall and precision. All evaluation metrics are described as follows:

$$\text{Precision} = \frac{TP}{TP + FP}$$

$$\text{Recall} = \frac{TP}{TP + FN}$$

$$F1 = 2 \times \frac{(\text{Recall} \times \text{Precision})}{(\text{Recall} + \text{Precision})} \tag{6}$$

where TP is the true positive, which correctly indicates the presence of the result, and FP is the false positive, which correctly predicts the absence of the result. The FN incorrectly predicts the result of absence.

Fig. 4 illustrates the detection results (represented by the red line) of various types of surface ruptures created by the earthquake, as obtained from raw satellite images (Top row), using the proposed model. The second row displays the initial mapping results, while the third row depicts the refined mapping results that are additionally generated from the initial image to show the real crack shape and to compare with the predicted result in the test set.

As shown in the satellite images in Fig. 4(a)–(c), it can be observed that there are features, such as roads or dried rivers that appear similar to cracks. However, in the results of the developed
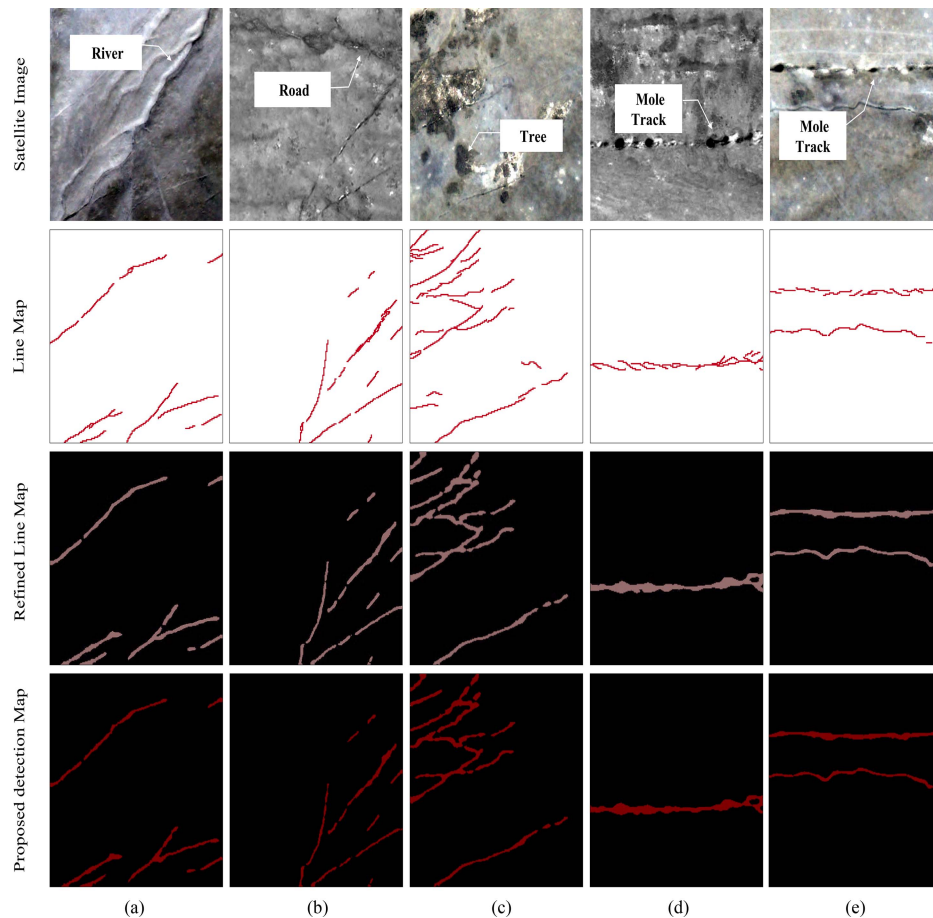
Fig. 4. Examples of the crack detection result by proposed and line maps as ground truth. 1st row: satellite image, 2nd row: initial line map, 3rd row: refined line map and 4th row: proposed detection map.

model, it is apparent that it only detects surface ruptures and does not detect these similar structures. Compared to the ground truth, slight differences in the thickness or disconnection of the cracks are visible; however, the model can detect complex structures, even very small cracks, accurately. In addition, the model accurately detects irregular surface ruptures, such as the mole track and tension crack, as shown in Fig. 4(d)–(e). Notably, the line map used for training does not fully represent these types of cracks, yet the developed model is able to detect them in their original form, as seen in the refined map. Fig. 4 demonstrates that the proposed model can robustly represent the real rupture shape even in harsh conditions and similar structures, such as dried-up rivers and roads.

Meanwhile, in this study, a quantitative comparison was conducted with several models, as illustrated in Fig. 5. The goal was to determine how differences in the detection target, training dataset configuration, and image source (satellite) affect the detection results. For this purpose, we compared the results of existing line detector models (Sobel edge [30] and GVG detector [31]), as well as deep learning-based crack detection models (Deep Crack [32], CrackSegNet [33], and Crack-CADNet [23]) to the model we used. However, some models are designed to detect crack datasets on road surfaces based on general images, while others are designed to detect surface ruptures captured

through UAVs, making it impossible to evaluate performance based on the same standards as our model.

The two line/edge detectors in Fig. 5 exhibited inferior performance in extracting edges or cracks compared to other models. This is because these detectors were developed to detect edges or cases where gradients occur in the image due to clear changes in relief or terrain structure. Nevertheless, in Fig. 5(b), some visible cracks were successfully detected, while in Fig. 5(d), the outlined road was excluded while effectively capturing the fine cracks on the right side. In contrast, models based on deep learning demonstrated notable crack detection capabilities. Deep crack, as shown in Fig. 5(c), captures even complex cracks in detail. However, there was a tendency to misclassify terrain features, such as rivers and roads as cracks. This is because the model was developed to detect cracks in environments, such as roads and buildings. On the other hand, models, such as CrackSegNet or Crack-CADNet incorrectly identified certain rivers, as shown in Fig. 5(a). However, they showed accurate detection of major cracks in Fig. 5(b). In addition, even though both models were developed for the detection of building ruptures or UAV-based local areas, they successfully avoided mistaking the road as a crack in Fig. 5(d), ensuring the detection performance of all apparent ruptures. Meanwhile, our proposed model is the only model that can accurately detect cracks without
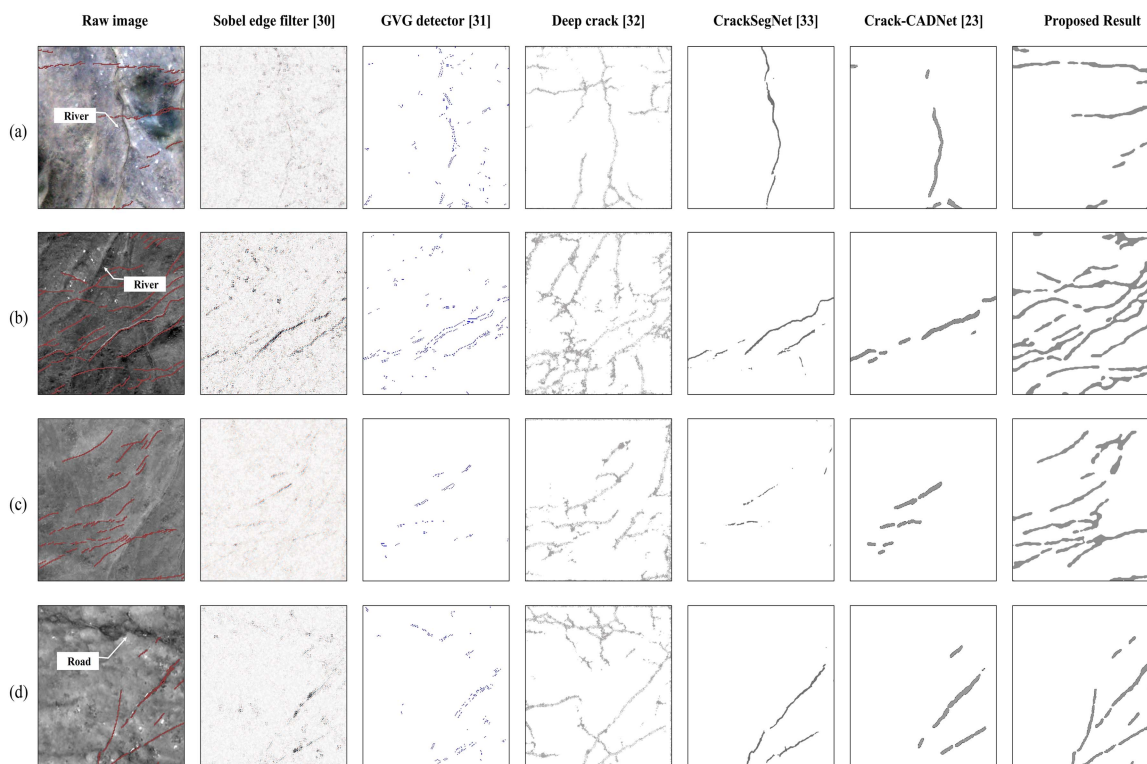
Fig. 5.   Detection performance comparisons of the proposed method with other detection methods: 1st column: satellite image with the ground truth (red line) overlaid, 2nd–6th columns: results predicted by different models.

misidentifying the road, as shown in Fig. 5(a), and can accurately detect complex cracks, as shown in Fig. 5(b). This can be interpreted as the result of configuring the data set to detect various types of surface ruptures that we target, and effectively training the model to reflect the characteristics of the satellite images as much as possible. The final performance of the proposed model is as follows: 90.46% precision, 85.57 % recall, and 87.95 % F1 score.

B. Large-Scale Surface Rupture Detection

As seen in the previous section, the detection result is interpreted as mapping the result of surface rupture by the earthquake. The mapping results for the central-western part of the Bulnay fault and the Dungen fault are presented in this section, with various rupture geometries shown in Fig. 1(c) and (d); therefore, to analyze this area, large-scale test regions are required. The proposed model was trained with fixed-size input images (512, 512); however, the model was designed to operate regardless of input size in the test process. The surface ruptures detected in the central-western section of the Bulnay fault have complex but typical geometries that are associated with strike-slip earthquakes (e.g., [34]), as highlighted in Fig. 6(a)–(d). The size of Fig. 6(a)–(f) is huge, with a range from 2000–3000 pixels, and each size is different.

The main rupture strand is distinguishable in most parts of the rupture section due to en echelon arrays of subsidiary ruptures and cracks. The azimuth of the main rupture zone varies from 90° to 100° east from the north, and the width of the main rupture zone is also variable. The subsidiary ruptures are often subparallel to the azimuth of the main rupture. In addition, the main rupture generally displays a stepping geometry, even with a variable stepping distance. Secondary ruptures were highly distributed around the main rupture zone, particularly around the fault-stepping area. Most of these detection results by the proposed model correspond with those of previous investigations ([1], [35]). It is worth noting that along-fault variations in rupture geometry along with offset distribution are indicators of segmented-fault geometry, which is closely related to dynamic earthquake rupture propagation.

We applied the proposed model to detect discontinuity cracks in the Dungen fault, which is primarily characterized by en echelon cracks without a through-going rupture trace [see Fig. 6(e) and (f)]. Our results reveal that the rupture consists of a series of NE–SW trending cracks. The majority of individual cracks exhibit a sharp geometry, indicative of Mode-I tension cracks, while only some of the ruptures display a rightward curve at both tips, indicating a dextral slip. Rupture is frequently characterized by a combination of en echelon cracks and mole tracks that are orthogonal to one another. In a later section, we will discuss detailed quantitative analysis results, such as crack length and thickness. Many of these geometrical patterns closely resemble previous findings [1].

C. Morphology Feature Analysis Model and Performance

After completing the mapping of the rupture, the morphological properties of the extracted rupture are analyzed. In particular,
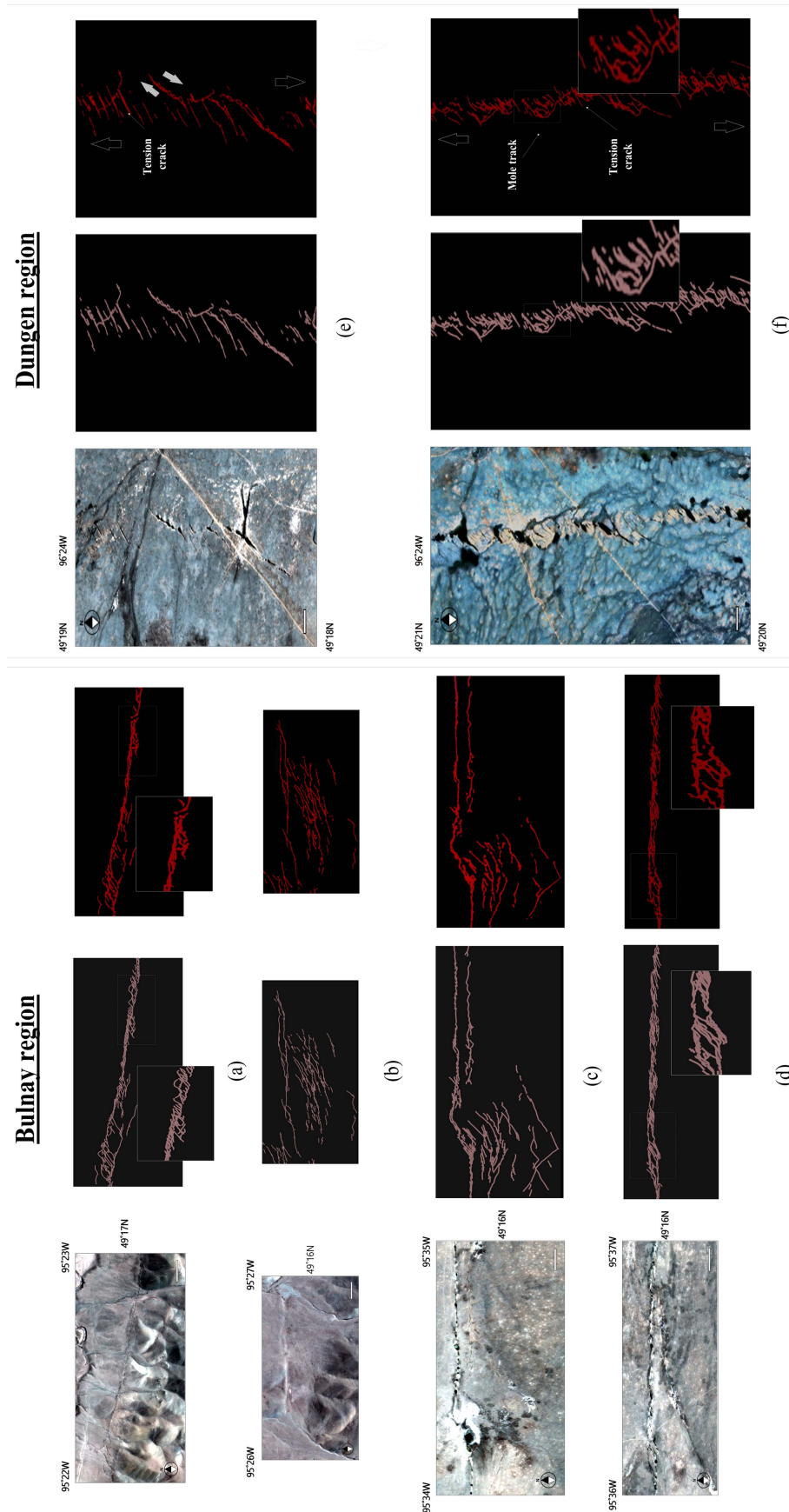
Fig. 6. Surface rupture detection result on test sites of the Bulnay and Dungen region.
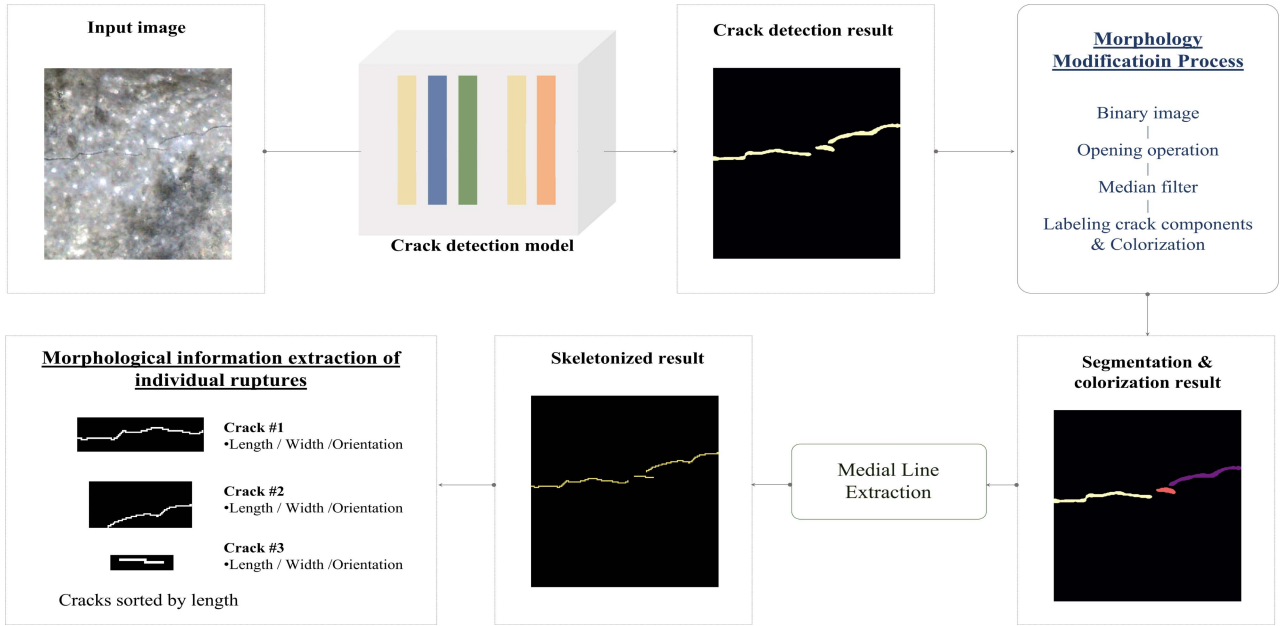
Fig. 7.   Schematic diagram of the proposed crack morphology analysis.

quantitative analysis of the ruptures, including length, average width, orientation, and location (coordinates), plays an important role in precisely identifying earthquake-induced ruptures. To achieve this, we developed a morphological analysis model that converts the detected cracks in the image into individual cracks and extracts their geometric information.

The morphology analysis is processed with segmentation, skeletonization step, and feature analysis, as shown in Fig. 7. Here, the skeleton is the result of the thinning process, also called the "medial axis," which was first proposed by [36]. The original 2-D shape in the image is changed to a skeleton graph while maintaining the original geometric and topological information. Skeleton images in the field of geology/geomorphology enable the structural state analysis of surface ruptures through topological visualization of surface ruptures. Several thinning algorithms have been studied to produce different skeleton shapes and applications.

After obtaining the rupture mapping result through the detection model, the image is first converted into a binary image whose pixels have only two possible intensity values (0,1), and then the opening operation is applied to that. The opening operation ($\circ$), defined in (7), is the dilation operation ($\oplus$) of erosion result in order to condense the cracks. Erosion ($\ominus$) is the process of eroding the object's borders, whereas dilation is the process of increasing the object's coverage, and the operation was performed on two sets of images: the original image I and a structural element M

$$I \circ M = (I \ominus M) \oplus M. \qquad (7)$$

Subsequently, the median filter, which is a nonlinear method for determining the median value within a specified window and removing outliers that are not among the sorted values [37], is adopted. After the application of the two morphological steps, the cracks are labeled as a single crack and assigned different colors, as shown in Fig. 7. The color-coded representation of these cracks allows for a rapid understanding of the total number of cracks and the complexity of their distribution. To ensure the accuracy of the model, a test area with highly detailed and complex cracks was selected, as shown in Fig. 8. As shown in the figure, counting the colors expressed in each image can confirm the complexity of how many cracks a region is divided into. Also, the skeleton line was accurately extracted while maintaining its original shape without distorting or changing the initial detection result. In particular, such a uniform width output image effectively identifies the segmental shape of cracks and predicts the direction of occurrence of the earthquake.

Morphological characteristics, such as the length and width of each crack, were calculated based on the segmentation and skeletonization results, as depicted in Fig. 9(a).

The first morphological characteristic analyzed is length. The length was calculated based on the one-pixel-with skeleton line, and as shown in Fig. 9(b), it was confirmed that the number of cases of line distribution in the (3×3) array is five. Therefore, the "total length ($length_i$)," which is the sum of all cases over each crack, is expressed by (8), where n_k represents the number of occupied pixels in cases C_k, and C_k represents the line distance in each configuration case in Fig. 9(b). Furthermore, k has a value between one and five

$$length_i = \sum_{i=1}^{5} \frac{n_k C_k}{2} + \frac{n_1 C_1 + n_2 C_2}{2}. \qquad (8)$$

The second property is the area, and each crack's total area ($area_i$) is calculated as the sum of the pixel values in the unskeletonized segmented image of the ith crack, as described in (9), and s_{xy} is the (x,y) pixel defined as a crack class at (x,y)

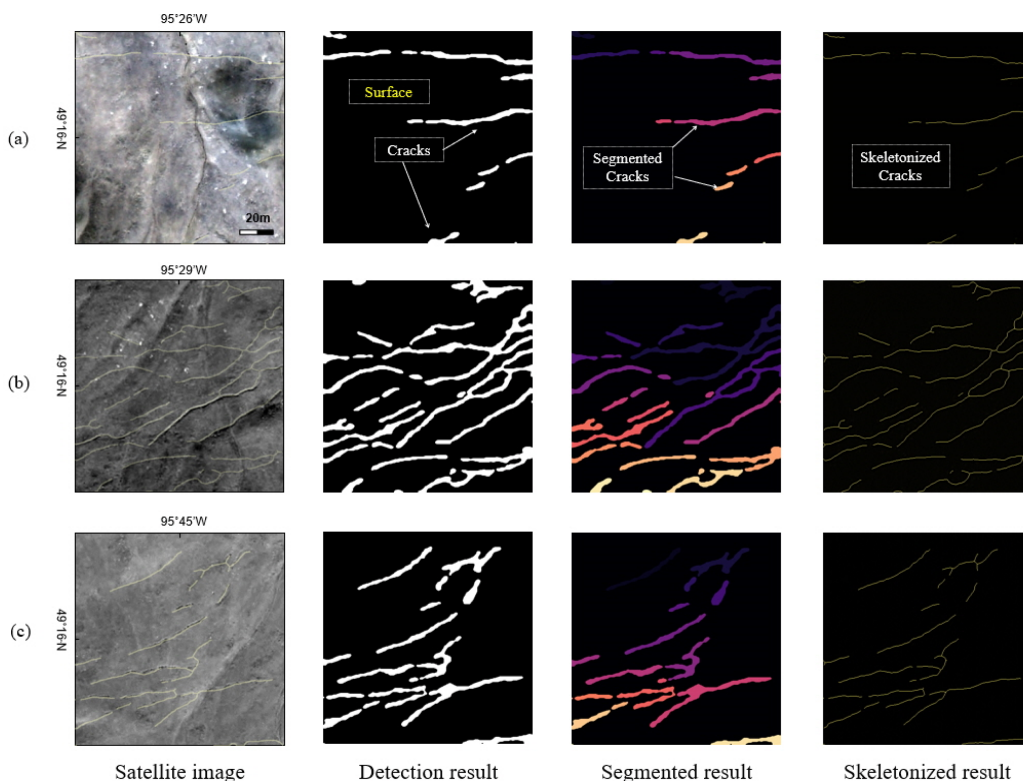$$area_i = \sum_{x,y} s_{xy}. \qquad (9)$$

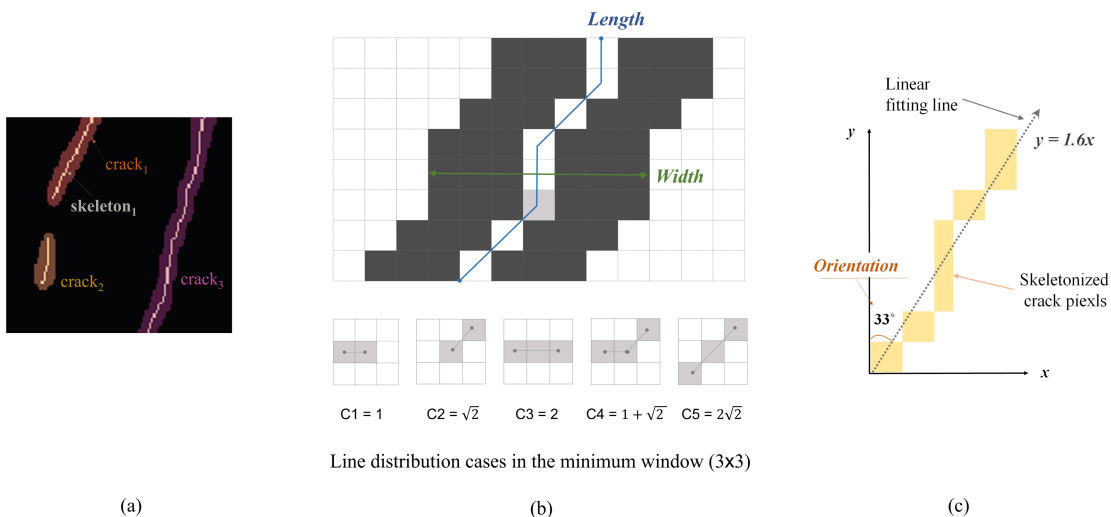Fig. 8. Example of crack segmentation and skeletonization result.

Fig. 9. Calculation of morphological features. (a) Individually segmented crack result. (b) Grid form for crack width and length calculation. (c) Crack orientation calculation.

On the other hand, the "*mean width*" of cracks was calculated as the ratio of area and length. And all the normal distances from the central line to the edge of the crack were calculated, and the longest value was defined as the "*maximum width*" of the crack.

We assume that the individual cracks in the skeleton image can be represented by an (x, y) curve starting at $(0,0)$, where the X-axis represents the east–west direction and the Y-axis represents the north–south direction. When the linear fitting is applied to each curve (crack), the slope (α) of the fitting result with respect to the Y-axis, as shown in Fig. 9(c), can be interpreted as the "*orientation*."

Fig. 10 shows the results of rupture mapping for the four test sites and the extraction of various morphological information described above. The reliability of the analysis obtained by the proposed method was confirmed by comparison with reference studies [1]. When compared to the entire test area, the length estimation showed an error <1 %, the width <3 %, and the
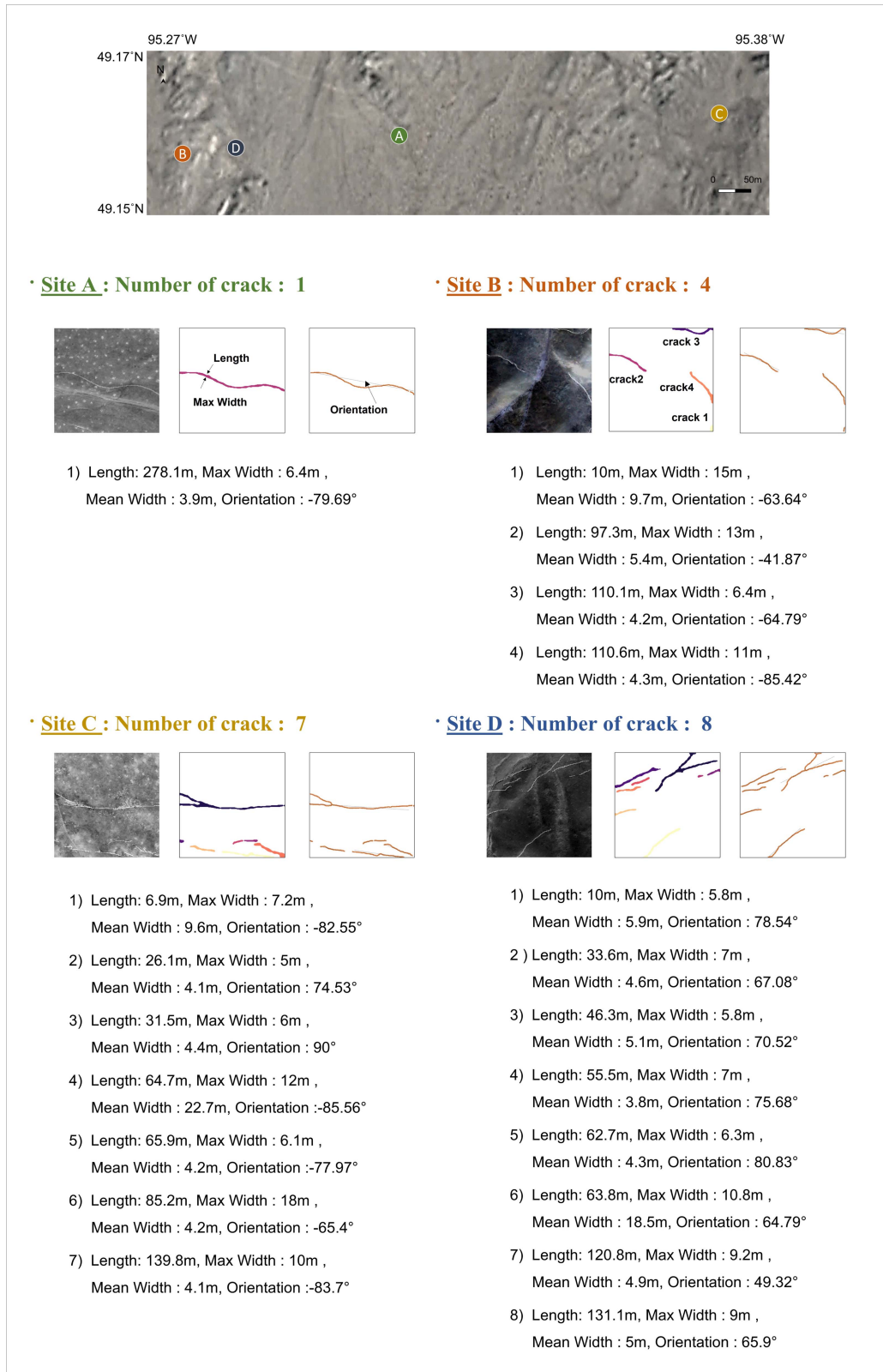
Fig. 10. Results of crack segmentation result with fitting line [Top: raw image, Middle: segmentation result, Bottom: skeleton line (red) with the fitting line (black)] and calculated morphological information of each crack.

orientation $< 3°$. All extracted cracks have coordinates, so their location can be identified, and all characteristics can be directly converted into a unit of [m].

D. Statistical Analysis and Results

One of the advantages of our crack detection and segmentation is that it allows standardized and rapid statistical analysis of the geometries of earthquake surface ruptures. Indeed, manual observations and visual measurements of all deformations can be labor-intensive and time-consuming, making deep learning an advantageous alternative. The results of this statistical analysis enable quantitative evaluation of distributed deformation and hence provide valuable information on the seismic behavior of fault ruptures [1], [15], [16]. In this study, we present the results of the statistical analysis of two rupture sections on the Dungen fault: the southern section [Fig. 6(e)] and the northern section [Fig. 6(f)], which are composed of en echelon cracks with no thoroughgoing rupture along the fault. For the targeted sections, the geometrical elements analyzed include number of cracks and each crack's azimuth, length, and width (mean, maximum). We note that the crack width is measured perpendicular to the azimuth of the crack, and hence it is an oblique parameter with respect to the general trend of the Dungen fault (north–south direction). Here, we test the amount of lateral offset using the projected crack width which is estimated by projecting the crack width onto the north–south direction, as proposed by [38].

In the southern section, which spans approximately 1.5 km, exhibited a total of 65 detected ruptures. The azimuth of each crack was predominantly northeast–southwest, with an average length of 53.2 m and a range of 10 to 150 m [Fig. 11(a)]. The projected maximum width showed high variability, with a lower limit of approximately 2.5 m, but the mean width of the ruptures was concentrated at approximately 3.5 m, which is evident in the lower limit [Fig. 11(b)]. In the northern section, we have identified 115 cracks, which is almost twice the number detected in the southern section, along with a fault that is approximately 2-km long [as depicted in Fig. 6(f)]. The azimuth of these cracks is predominantly northeast–southwest, with a few more of them being subperpendicular (i.e., NW–SE) to those cracks, as shown in Fig. 11(e). The average length of these cracks ($\sim$ 53.0 m) is comparable to that of the southern section, but their variability is higher, reaching up to 341 m [as illustrated in Fig. 11(e)]. On average, the projected width is about 4 m and generally narrower than 5 m. It is noteworthy that the along-fault variations in the crack width are relatively inconsistent when compared to those in the southern section. The relationship between the projected width and the other two geometrical elements, i.e., the azimuth and length of the cracks [Figs. 11(c), (d), (g), and (h)] indicate that there is no significant correlation between geometric factors of cracks. One notable result is that, in the northern section, the lower limit of the projected crack width tends to increase when the crack azimuth is closer to the main trend of the Dungen fault (north–south direction) [Fig. 11(h)].

Our statistical analysis has revealed the following differences between two fault sections: 1) The number of cracks, including those of cracks in the NW–SE direction, is higher in the northern section, 2) the lower limit of the crack width, which is proportional to the lateral offset, is wider in the northern section, and 3) the cracks in the northern section have high variations in along-fault crack width with a tendency to widen in the general trend of the main fault. This could be due to variations in the degree of connection between neighboring cracks, which may be linked to the amount of lateral deformation. It is important to note that the en echelon cracks in the northern section are mostly connected by northwest–southeast trending cracks, indicating a relatively well-linked rupture geometry [1]. Our results imply that the amount of surface deformation is lower to the south, where it approaches to the Bulnay rupture, and we interpret that there was a slip bump at a fault branch during the rupture propagation from the main Bulnay fault to the Dungen fault. Along the Dungen fault, Baljinnyam et al. [39] inferred 1–2 m of horizontal offset on average based on the dimensions of tension cracks, but without any quantitative measurement criteria. Our estimation of the lower limit of the projected crack width imply that horizontal offset of about 2.5 m in the last (1905) earthquake event. Although the wider crack width, that is larger offset, could be the result of cumulative deformations over multiple earthquakes, it is challenging to determine the origin of the offset since there have been no reported geomorphic and/or paleoseismological observations.

IV. DISCUSSION

A. Advance and Implications

To map in detail and shortly the distribution of surface deformation after an earthquake offers an opportunity to investigate seismic source fault [5], dynamic rupture propagation [1], [15] and surface displacement hazards [2], [3], [24]. As mentioned in the Section I-A, prior to the 1990s, the mapping of seismic surface ruptures primarily relied on field observations and aerial photograph analysis. Data collected in this manner required manual analysis or observations made during field visits to analyze variations and characteristics of the rupture geometry, which could be labor-intensive and time-consuming tasks. In recent years, high-resolution remote sensing data (such as satellite, drone, etc.) and high-quality topographic data (seismic and geological data) have been integrated with state-of-the-art analytical techniques to gain a multidimensional understanding of earthquakes [10], [11], [16]. Here, we propose solutions that incorporate deep learning and image processing techniques for automated imagery detection and analysis of the earthquake surface ruptures within imagery can serve as efficient tools for researchers.

Satellites acquire space imagery information for the entire Earth with centimeter-level high resolution on a periodic basis, enabling valuable applications in postearthquake damage assessment and rapid response strategy formulation. Particularly, the greatest advantage lies in the ability to swiftly obtain information about the earthquake surface ruptures for vast regions up to hundreds of kilometers long [7]. Indeed, in a few days later of the earthquake, particularly in humid and rainy regions, coseismic surface ruptures could be altered or removed due to meteorological conditions or on-site recovery operations following the
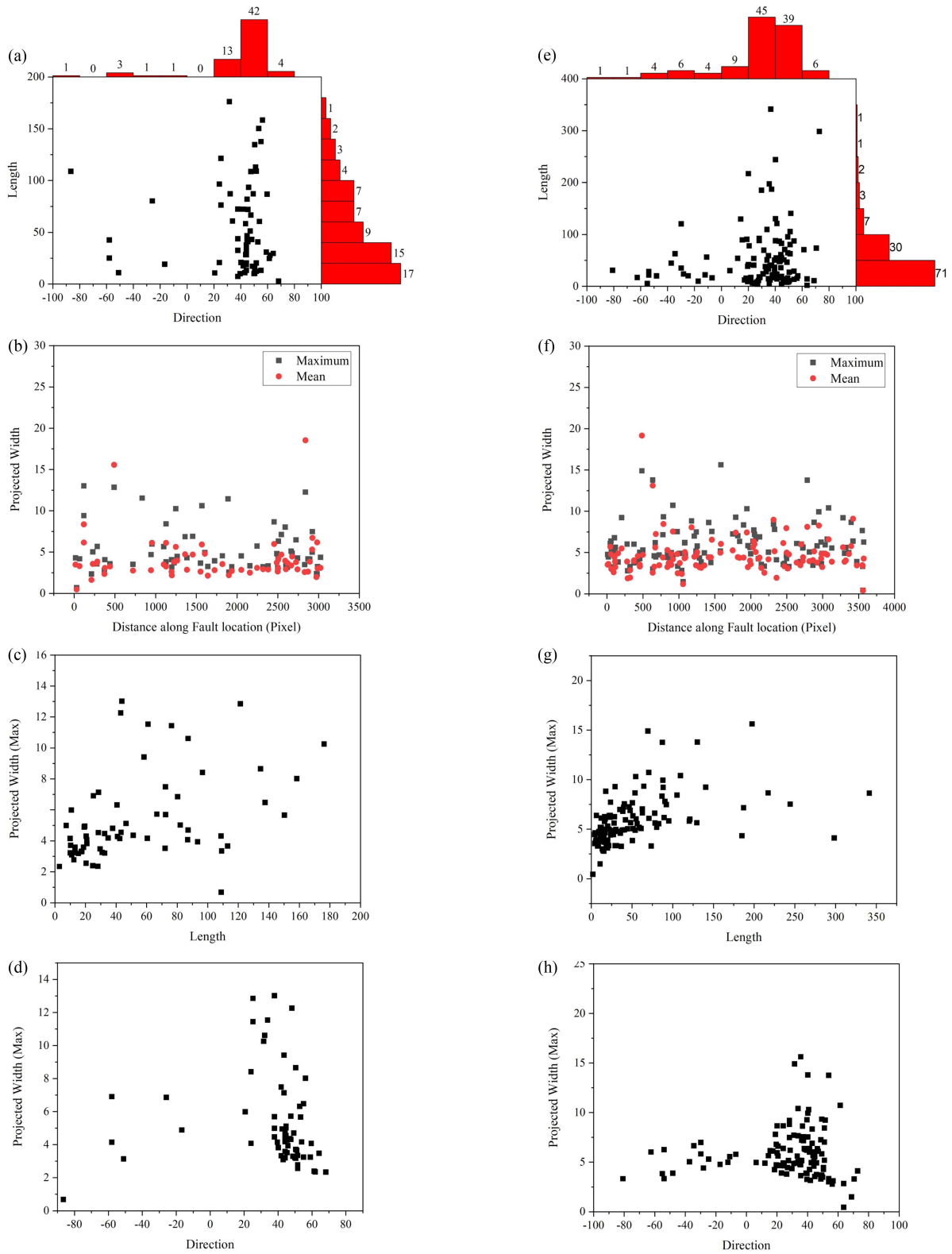
Fig. 11. Relationships between geometrical elements—azimuth, length (m), and projected width (m)—of each rupture and/or crack on the southern sections (a)–(d) and northern sections (e)–(h) of the Dungen fault are presented. The term "direction" has been replaced with "azimuth," and the Azimuth has been indicated with the addition of [from North to east (+) and to the west (-)] in parentheses.

seismic event. Combining high-resolution satellite imagery with state-of-the-art deep learning technology can provide related researchers with rapid, comprehensive, and objective information about surface ruptures, making it a valuable foundational resource for investigations of the fault-rupture.

This study proposes a deep learning-based one-stop solution model for the accurate detection and geometrical analysis of various forms of surface ruptures in high-resolution satellite imagery. The proposed model demonstrates the capability to clearly distinguish similar surface rupture forms in features, such as road, water system, and artificial structures. Various types of significant surface ruptures were detected with high performance by the proposed model, accurately mapping even intricate details of surface ruptures. Importantly, the proposed model can analyze large-scale distributed surface ruptures regardless of their shape or complexity within the resolution of satellite imagery. However, it should be noted that factors, such as weather conditions, vegetation distribution, and obstacles in satellite imagery can obscure surface ruptures, potentially leading to reduced detection rates.

On the other hand, we presented that a statistical analysis of rupture geometry, such as orientation, length, and width, extracted based on the detected cracks, provides insights into the rupture behavior using the case of two sections of the Dungen fault. This demonstrates that the proposed model not only validated the accuracy of the mapping but also delivered precise information at a detailed level for extensive areas. This can be attributed to the high-quality labeling dataset, which includes various types of surface ruptures, validated by experts, and the optimal training on this dataset. The outcomes of this statistical analysis play a crucial role in facilitating a quantitative assessment of variations in distribution of the surface deformation. By automating the detection and analysis processes, researchers can expedite their studies, reduce the potential for human and/or subjective bias, and ensure a more consistent and objective evaluation of characteristics of the earthquake surface ruptures. The objective observation could be an essential factor for building unified database of the earthquake surface ruptures and performing correlation analysis [7], [24]. This approach not only enhances the accuracy of data collection but also empowers researchers to make informed decisions and draw reliable conclusions about earthquake surface deformation. Overall, the integration of deep learning technology in surface rupture analysis represents a promising avenue for advancing our understanding of earthquake dynamics and improving earthquake hazard assessment.

Surface rupture mapping information for large-scale faults distributed globally primarily consists of georeferenced vector files manually created by experts in related research [24]. By utilizing this data, it becomes possible to integrate previously established ground truth data with satellite data of varying resolutions and characteristics. Furthermore, any necessary additions or missing information in the created ground truth data can be enhanced using various image processing techniques. When accuracy-enhanced information is used as train data, it can further improve the performance and robustness of the model. Recently, Li and Ren [40] introduced "EASRAPP," a Python-based semiautomatic application that can be used on personal computers and the web. This application utilizes feature extraction in the HSV color space to classify and extract surface ruptures, providing a fast method for extracting detailed structures of cracks or fractures in high-resolution remote sensing images. EASRAPP is expected to serve as a practical tool to support the training of deep learning models by providing sample datasets for geologists and geophysicists.

B. Limitations and Future Directions

There are plans to address and improve the constraints imposed by the use of satellite imagery to enhance the model's performance. The limitations associated with satellite imagery, including resolution constraints and variations in viewing angles, can reduce the clarity of surface features of interest. In addition, factors like cloud cover and seasonal changes (e.g., snow and vegetation) can significantly decrease visibility and accuracy in feature extraction. These challenges underscore the need for innovative approaches and techniques to mitigate these limitations and improve the accuracy of surface rupture detection models in satellite imagery. Environmental constraints, such as limitations in satellite image resolution, changes in viewing angles, and factors like noise and shadows within the imagery, are common challenges faced by researchers analyzing remote sensing-based images. Therefore, obtaining time-series data that encompass seasonal variations and different viewing angles is crucial, allowing the model to learn from a wide range of environments. In addition, synthesizing multimodal data, including data from UAVs with varying resolutions or different wavelength DEM and synthetic aperture radar (SAR) data, can be a viable approach. These strategies can enhance the model's robustness and its ability to mitigate noise and other environmental constraints, ultimately improving the accuracy of surface rupture detection. However, it is not just the data source but also the reliability of the ground truth that must be ensured. The labeling dataset of this study was obtained through expert review, but it may still contain some level of uncertainty. Ground truth labeling information for surface ruptures can vary depending on the resolution of the data source used by experts and may even differ based on individual expert opinions. Therefore, the creation and availability of mapping validation data on a global scale for large-scale faults, based on objective and consistent criteria, would significantly reduce the uncertainty associated with surface rupture detection models and play a role of a highly valuable common reference source. To address these limitations and uncertainties, further research and efforts are indeed necessary. Our study aims to contribute to the improvement of research directions in this field by providing an integrated solution for surface rupture detection and analysis, building upon previous research efforts. We anticipate that this research will significantly advance the field of surface crack detection and analysis by effectively addressing these challenges and offering valuable insights for the development of more robust and accurate models. In addition, in this study, instead of considering detailed surface rupture information from existing validation data, a binary classification approach was applied to

the model, distinguishing between "surface rupture" and "non-surface rupture," from a general perspective. In the future, there are plans to utilize various ground truth labels to further segment surface ruptures and perform multiclass classification based on different types of surface ruptures. The goal is to harness the capabilities of the latest deep learning models to understand structural characteristics, such as fault growth, organization, mechanics, and seismic potential at the surface fault level.

V. CONCLUSION

This research deserves attention for introducing a fit-for-purpose approach to detect and analyze earthquake surface ruptures using high-resolution satellite images. This approach places particular emphasis on accurately detecting surface ruptures caused by earthquakes by utilizing a high-performance deep learning-based crack detection model. In addition, the study introduces a model for the automated analysis of the geological and geomorphological characteristics associated with the detected cracks. The model guarantees the flexibility of test size and derives an immediate analysis result in a large-scale area. A learning strategy applying random augmentation and penalty loss confirmed that all of the various verification showed high performance. The reliability of the model was confirmed through comparative verification with actual surface rupture investigations. As a result, it can serve as an automated and comprehensive solution for rapidly and precisely mapping and quantitatively analyzing earthquake surface ruptures. This can aid in improving our understanding of the geometrical complexity and relationships in rupture behaviors along inherited fault systems. Furthermore, by utilizing time-series satellite images for periodic visits and data acquisition, the proposed model may enable automatic evaluation of the degree of risk associated with destructive earthquakes, including recent events, such as the 2023 Turkey–Syria earthquake and the 2022 Qinghai earthquake. This can provide basic spatial data on surface ruptures to field researchers and modelers, as well as suggest future evaluation plans for earthquake-prone areas.

ACKNOWLEDGMENT

REFERENCES

[1] J.-H. Choi et al., "Geologic inheritance and earthquake rupture processes: The 1905M 8 Tsetserleg-Bulnay strike-slip earthquake sequence, Mongolia," *J. Geophysical Res.: Solid Earth*, vol. 123, no. 2, pp. 1925–1953, 2018.

[2] W. Lettis et al., "Influence of releasing step-overs on surface fault rupture and fault segmentation: Examples from the 17 August 1999 Izmit earthquake on the north anatolian fault, Turkey," *Bull. Seismological Soc. Amer.*, vol. 92, no. 1, pp. 19–42, 2002.

[3] S. G. Wesnousky, "Predicting the endpoints of earthquake ruptures," *Nature*, vol. 444, no. 7117, pp. 358–360, 2006.

[4] D. P. Schwartz and K. J. Coppersmith, "Fault behavior and characteristic earthquakes: Examples from the Wasatch and San Andreas fault zones," *J. Geophysical Res.: Solid Earth*, vol. 89, no. B7, pp. 5681–5698, 1984.

[5] K. Sieh et al., "Near-field investigations of the Landers earthquake sequence, April to July 1992," *Science*, vol. 260, no. 5105, pp. 171–176, 1993.

[6] Y. Awata, "Explanatory text of the strip map of the surface fault ruptures associated with the 1995 Hyogo-Ken Nanbu earthquake, central Japan the Nojima, Ogura and Nadagawa earthquake faults-, scale 1: 10,000," Geological Surv. Jpn., AIST, Tosu, Japan, Tectonic Map Series 12, 1998.

[7] D. L. Wells and K. J. Coppersmith, "New empirical relationships among magnitude, rupture length, rupture width, rupture area, and surface displacement," *Bull. Seismological Soc. Amer.*, vol. 84, no. 4, pp. 974–1002, 1994.

[8] J. P. McCalpin and E. M. Gath, "50 years of paleoseismology: The science and the business," *AEG News*, vol. 64, 2021, Art. no. 3.

[9] C. L. Glennie, W. E. Carter, R. L. Shrestha, and W. E. Dietrich, "Geodetic imaging with airborne LiDAR: The Earth's surface revealed," *Rep. Prog. Phys.*, vol. 76, no. 8, 2013, Art. no. 086801.

[10] O. Zielke, Y. Klinger, and J. R. Arrowsmith, "Fault slip and earthquake recurrence along strike-slip faults—contributions of high-resolution geomorphic data," *Tectonophysics*, vol. 638, pp. 43–62, 2015.

[11] J. Elliott, R. Walters, and T. Wright, "The role of space-based observation in understanding and responding to active tectonics and earthquakes," *Nature Commun.*, vol. 7, no. 1, 2016, Art. no. 13844.

[12] S. Leprince, S. Barbot, F. Ayoub, and J.-P. Avouac, "Automatic and precise orthorectification, coregistration, and subpixel correlation of satellite images, application to ground deformation measurements," *IEEE Trans. Geosci. Remote Sens.*, vol. 45, no. 6, pp. 1529–1558, Jun. 2007.

[13] A.-M. Rosu, M. Pierrot-Deseilligny, A. Delorme, R. Binet, and Y. Klinger, "Measurement of ground displacement from optical satellite image correlation using the free open-source software micmac," *ISPRS J. Photogrammetry Remote Sens.*, vol. 100, pp. 48–59, 2015.

[14] C. P. Scott, J. R. Arrowsmith, E. Nissen, L. Lajoie, T. Maruyama, and T. Chiba, "The M7 2016 kumamoto, Japan, earthquake: 3-D deformation along the fault and within the damage zone constrained from differential lidar topography," *J. Geophysical Res.: Solid Earth*, vol. 123, no. 7, pp. 6138–6155, 2018.

[15] A. Vallage, Y. Klinger, R. Lacassin, A. Delorme, and M. Pierrot-Deseilligny, "Geological structures control on earthquake ruptures: The mw7. 7, 2013, Balochistan earthquake, Pakistan," *Geophysical Res. Lett.*, vol. 43, no. 19, pp. 10–155, 2016.

[16] S. L. Antoine, Y. Klinger, A. Delorme, K. Wang, R. Bürgmann, and R. D. Gold, "Diffuse deformation and surface faulting distribution from submetric image correlation along the 2019 Ridgecrest, California, ruptures," *Bull. Seismological Soc. Amer.*, vol. 111, no. 5, pp. 2275–2302, 2021.

[17] L. Mattéo et al., "Automatic fault mapping in remote optical images and topographic data with deep learning," *J. Geophysical Res.: Solid Earth*, vol. 126, no. 4, 2021, Art. no. e2020JB021269.

[18] O. Ronneberger, P. Fischer, and T. Brox, "U-net: Convolutional networks for biomedical image segmentation," in *Proc. 18th Int. Conf. Med. Image Comput. Comput.-Assist. Interv.*, Munich, Germany, 2015, pp. 234–241.

[19] O. Tasar, Y. Tarabalka, and P. Alliez, "Incremental learning for semantic segmentation of large-scale remote sensing data," *IEEE J. Sel. Topics Appl. Earth Observ. Remote Sens.*, vol. 12, no. 9, pp. 3524–3537, Sep. 2019.

[20] B. Jafrasteh, I. Manighetti, and J. Zerubia, "Generative adversarial networks as a novel approach for tectonic fault and fracture extraction in high resolution satellite and airborne optical images," *ISPRS-Int. Arch. Photogrammetry Remote Sens. Spatial Inf. Sci.*, vol. 43, 2020, pp. 1219–1227.

[21] B. Kanoun, M. A. Cherif, I. Manighetti, Y. Tarabalka, and J. Zerubia, "An enhanced deep learning approach for tectonic fault and fracture extraction in very high resolution optical images," in *Proc. IEEE Int. Conf. Acoust. Speech Signal Process.*, 2022, pp. 3403–3407.

[22] X. Chen, G. Hu, and X. Liu, "Recognition of earthquake surface ruptures using deep learning," *Appl. Sci.*, vol. 12, no. 22, 2022, Art. no. 11638.

[23] D. Yu, S. Ji, X. Li, Z. Yuan, and C. Shen, "Earthquake crack detection from aerial images using a deformable convolutional neural network," *IEEE Trans. Geosci. Remote Sens.*, vol. 60, 2022, Art. no. 4412012.

[24] S. Baize et al., "A worldwide and unified database of surface ruptures (SURE) for fault displacement hazard analyses," *Seismological Res. Lett.*, vol. 91, no. 1, pp. 499–520, 2020.

[25] P. Molnar and P. Tapponnier, "Cenozoic tectonics of asia: Effects of a continental collision: Features of recent continental tectonics in asia can be interpreted as results of the India-Eurasia collision," *Science*, vol. 189, no. 4201, pp. 419–426, 1975.

[26] P. Tapponnier and P. Molnar, "Active faulting and cenozoic tectonics of the Tien Shan, Mongolia, and Baykal regions," *J. Geophysical Res.: Solid Earth*, vol. 84, no. B7, pp. 3425–3459, 1979.

[27] K. Simonyan and A. Zisserman, "Very deep convolutional networks for large-scale image recognition," 2014, *arXiv:1409.1556*.

[28] J. Long, E. Shelhamer, and T. Darrell, "Fully convolutional networks for semantic segmentation," in *Proc. IEEE Conf. Comput. Vis. Pattern Recognit.*, 2015, pp. 3431–3440.

[29] E. D. Cubuk, B. Zoph, J. Shlens, and Q. V. Le, "Randaugment: Practical automated data augmentation with a reduced search space," in *Proc. IEEE/CVF Conf. Comput. Vis. Pattern Recognit. Workshops*, 2020, pp. 702–703.

[30] N. Kanopoulos, N. Vasanthavada, and R. L. Baker, "Design of an image edge detection filter using the Sobel operator," *IEEE J. Solid-State Circuits*, vol. 23, no. 2, pp. 358–367, Apr. 1988.

[31] R. Grompone, J. Jakubowicz, J. Morel, and G. Randall, "LSD: A line segment detector, image processing on line," *Image Process. On Line*, vol. 2, 2012, Art. no. 35.

[32] Y. Liu, J. Yao, X. Lu, R. Xie, and L. Li, "Deepcrack: A deep hierarchical feature learning architecture for crack segmentation," *Neurocomputing*, vol. 338, pp. 139–153, 2019.

[33] Y. Ren 1et al., "Image-based concrete crack detection in tunnels using deep fully convolutional networks," *Construction Building Materials*, vol. 234, 2020, Art. no. 117367.

[34] J. Tchalenko and N. N. Ambraseys, "Structural analysis of the Dasht-E Bayaz (Iran) earthquake fractures," *Geological Soc. Amer. Bull.*, vol. 81, no. 1, pp. 41–60, 1970.

[35] M. Rizza et al., "Earthquake geology of the Bulnay fault (Mongolia)," *Bull. Seismological Soc. America*, vol. 105, no. 1, pp. 72–93, 2015.

[36] H. Blum, "A transformation for extracting new descriptions of shape," in *Models for the Perception of Speech and Visual Form*. Cambridge, MA, USA: MIT Press, 1967, pp. 362–380.

[37] T. Huang, G. Yang, and G. Tang, "A fast two-dimensional median filtering algorithm," *IEEE Trans. Acoustics, Speech, Signal Process.*, vol. 27, no. 1, pp. 13–18, Feb. 1979.

[38] Y. Benjelloun et al., "Analysis of surface rupture complexity sheds light on coseismic slip during the last earthquakes along the Bulnay-tsetserleg fault zone (Mongolia)," *Copernicus Meetings*, 2020.

[39] I. Baljinnyam, *Ruptures of Major Earthquakes and Active Deformation in Mongolia and Its Surroundings*, vol. 181, Boulder, CO, USA: Geological Society of America, 1993.

[40] D. Li and J. Ren, "EASRAPP An open-source semiautomatic python GUI-based application for extraction and analysis of surface ruptures in a large earthquake," *Seismological Res. Lett.*, vol. 94, no. 4, pp. 2014–2029, 2023.

Yire Choi received the Ph.D. degree in geophysical exploration from the University of Science and Technology, Daejeon, South Korea, in 2018.

He is a Senior Researcher with the Active Tectonics Research Center, Korea Institute of Geoscience and Mineral Resources, Daejeon, South Korea. His research interests include paleogeography, remote sensing image processing, deep learning, and its applications.

Jin-Hyuck Choi received the Ph.D. degree in structural geology from Pukyong National University, Busan, South Korea, in 2014.

He is a Senior Researcher with the Active Tectonics Research Center, Korea Institute of Geoscience and Mineral Resources, Daejeon, South Korea. His research interests include history of paleo-earthquakes in a segmented active fault system and its implications for earthquake hazard assessment and also fault detection and evolution, active tectonics, earthquake geology, and paleoseismology.

Yeonju Choi received the Ph.D. degree in physics from Korea Advanced Institute of Science and Technology, Daejeon, South Korea, in 2014.

She is Senior Researcher with Satellite Application Division, Korea Aerospace Research Institute, Daejeon, South Korea. Her research interests include deep learning and its applications on remote sensing data processing and analysis.